Modulated spatial transmission signals in the photonic bandgap

Wenqi Xu(许文琪)[1], Hui Wang(王慧)[2], Daohong Xie(谢道鸿)[1], Junling Che(车俊岭)[1,†], and Yanpeng Zhang(张彦鹏)[3]

[1] *School of Science, Xi'an University of Posts and Telecommunications, Xi'an* 710121, *China*

[2] *School of Communication and Information Engineering, Xi'an University of Posts and Telecommunications, Xi'an* 710121, *China*

[3] *Key Laboratory for Physical Electronics and Devices of the Ministry of Education & Shaanxi Key Laboratory of Information Photonic Technique, Xi'an Jiaotong University, Xi'an* 710049, *China*

(Received 30 March 2022; revised manuscript received 30 May 2022; accepted manuscript online 8 June 2022)

This paper describes the spatial transmission of electromagnetically induced transparency and four-wave mixing signals in the photonic bandgap structure, which are modulated using the adjustable parameters of light fields. The spatial transmission patterns of the relevant signals are experimentally investigated with respect to the optical nonlinear Kerr effect that occurs in the modulation process. The experimental results reveal the spatial transmission patterns of the probe transmission and the four-wave mixing signals, such as focusing, defocusing, shifting, and spatial splitting. This study explains how the tunable parameters of light fields and their interactions with each other can regulate the spatial transmission of the light fields by changing the refractive indices of media, which provides a new research perspective and a degree of experimental technology support for more efficient all-optical communications.

Keywords: electromagnetically induced transparency, nonlinear Kerr effect, four-wave mixing, photonic bandgap

PACS: 42.65.–k, 42.50.Gy, 78.47.nj **DOI:** 10.1088/1674-1056/ac76b3

1. Introduction

For a long time, light field modulation — which mainly uses lasers to modulate various mesoscopic systems — has been a key area of optics research. In this modulation process, the interaction between laser light and materials and the resulting effects shed light on the workings of mesoscopic systems.[1] In addition, the related phenomena and effects have potential applications in light fields. Optical lattices constructed using artificial light fields are very important for light field modulation due to their unique periodic structure.[2] A periodic refractive index is formed when laser beams are transmitted in a periodic structure.[3] By periodically modulating the refractive index of the medium, the way in which a light field is transmitted by the medium can be adjusted to control and manipulate the light field. In this paper, we describe the implementation of an artificially tunable one-dimensional optical bandgap lattice that uses enhanced optical nonlinear effects based on electromagnetically induced transparency and the interactions of nonperiodically structured atoms.[4–6] Tunable spatial transmissions of light fields were implemented in such an optical bandgap lattice, and its transmission patterns were investigated by modulating the nonlinear Kerr effect. This provides another way to observe the spatial transmission properties of light fields, which provides a basis for better controlling and manipulating lasers to modulate the refractive indices of media. Such research has potential applications in all-optical communications,[7,8] as it enables the spatial transmission mode, logic, and relevance of a light field to be modulated.

The electromagnetically induced transparency effect offers great value for applications in nonlinear optics. In particular, when based on the multienergy atomic structure, electromagnetically induced transparency can not only drastically change the nonlinear refractive index of an atomic medium, which leads to a slower velocity of the probe beam, but can also enhance the nonlinear effect of the atomic medium and thus improve the intensity of the four-wave mixing signal.[9–11] In addition, the electromagnetically induced transparency effect can also enhance the nonlinear self-Kerr effect as well as the nonlinear cross-Kerr effect.[12,13] Furthermore, an electromagnetically induced grating can be created using the electromagnetically induced transparency phenomenon under certain spatial light field conditions,[14,15] causing the medium to form a periodic photonic bandgap structure.[16,17] In our experiment, we investigated the optical nonlinear Kerr effect generated by the electromagnetically induced transparency signal and the four-wave mixing signal in a one-dimensional photonic band structure. In this process, we observed the nonlinear Kerr effect and the corresponding transmission spot changes of two signals under different conditions, in particular, under the effect of interaction between different light fields. In addition, regulation of specific physical phenomena in the spatial images of the probe signal and the four-wave mixing signal was observed, including focusing, defocusing,[18] shifting,[19] and spatial splitting.[20] The experimental results show that the interaction between the light field and the medium can regulate the spatial transmission of the light field by changing the refractive index of the

†Corresponding author. E-mail: junling.che@163.com

© 2022 Chinese Physical Society and IOP Publishing Ltd

medium. These results provide experimental technology support for all-optical communications and open up potential research prospects for all-optical signal processing.

2. Experimental scheme

As shown in Fig. 1(a1), the energy levels in this experiment are designed based on an inverted Y-type four-energy atomic structure consisting of $5S_{1/2}(F=3)$ ($|0\rangle$), $5S_{1/2}(F=2)$ ($|3\rangle$), $5P_{3/2}$ ($|1\rangle$), and $5D_{5/2}$ ($|2\rangle$) in a rubidium (^{85}Rb) atomic four-energy system. The probe laser beam $\boldsymbol{E}_1$ excites $|0\rangle$ to $|1\rangle$, the coupling laser beams $\boldsymbol{E}_3$ and $\boldsymbol{E}_3'$ connect $|3\rangle$ and $|1\rangle$ from two opposite directions, and the external dressing laser beam $\boldsymbol{E}_2$ excites $|1\rangle$ to $|2\rangle$. As the light field excites the atoms to their respective energy levels, the mutual dressing effect between the energy levels causes individual energy levels to split and form the dark state, which results in the electromagnetically induced transparency phenomenon. Figure 1(a2) shows the relationship between the mutual dressing effects of individual energy levels. The light field $\boldsymbol{E}_3$ splits energy level $|1\rangle$ into two dressed states denoted by $|\boldsymbol{G}_3(z)+\rangle$ and $|\boldsymbol{G}_3(z)-\rangle$. When the external dressing field laser beam $\boldsymbol{E}_2$ is injected, the energy level $|\boldsymbol{G}_3(z)+\rangle$ is further split into two dressed states denoted by $|\boldsymbol{G}_3(z)+\boldsymbol{G}_2+\rangle$ and $|\boldsymbol{G}_3(z)+\boldsymbol{G}_2-\rangle$ due to the dressing effect between the energy levels. Figure 1(b) shows a schematic diagram of the experimental beam structure. The experimental setup is shown in Fig. 1(c); it consists of the probe laser beam $\boldsymbol{E}_1$ together with the coupling laser beams $\boldsymbol{E}_3$ and $\boldsymbol{E}_3'$. In addition, the oval part of the figure represents the rubidium medium inside a heated cavity. The laser beam is divided into multiple beams through different polarizing beam splitters (PBSs), and is focused into the atomic medium in different directions. After passing through the atomic medium, the laser beam is then injected into the charge-coupled device (CCD) and the oscilloscope through the optical attenuator. The evolution of the spatial beam and its regulation are observed using the signals in the CCD and the oscilloscope. First, different laser beams are injected into the system under different experimental conditions. PBS2 and PBS3 transmit the refracted probe transmission signal ($\boldsymbol{E}_\mathrm{P}$) to receiver D_1, while the four-wave mixing signal ($\boldsymbol{E}_\mathrm{F}$) is transmitted in the other direction through PBS1 and also through PBS4 to receiver D_2 and the CCD. The light fields $\boldsymbol{E}_1$ and $\boldsymbol{E}_3$ are injected in different directions, forming a small angle between them; $\boldsymbol{E}_3'$ is transmitted in the opposite direction to that of $\boldsymbol{E}_1$, while the dressing field $\boldsymbol{E}_2$ propagates at a small angle in the opposite direction to that of $\boldsymbol{E}_1$. In this process, the excitation energy levels of the periodic beam form a periodic split energy level structure, enabling a periodic polarization rate to be obtained, thus creating a periodic refractive index in the medium that finally constructs the photonic bandgap structure. The spectral signal in the detector and the spot image signal in the CCD are then observed and analyzed by changing the light field to adjust various parameters.

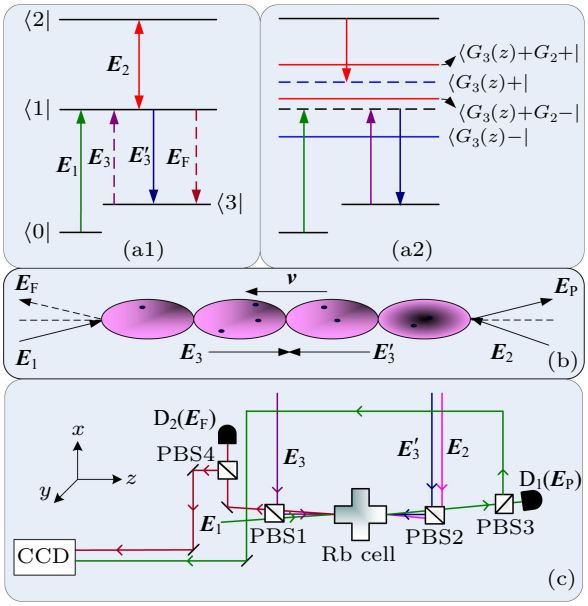


Fig. 1. (a1) Model of a four-energy atomic system and the energy level structure of the light field, (a2) diagram of the energy levels splitting under the effect of the dressing light field, (b) schematic diagram of the optical path design and the atomic medium, (c) diagram of the simple experimental setup, including PBS (a polarizing beam splitter), D_1 (detector 1), D_2 (detector 2), Rb cell (a rubidium cell), and CCD (a charge-coupled device).

3. Theoretical model

The self-Kerr and cross-Kerr effects are mainly generated by the interaction of the light field with the atomic medium. In order to help the reader to understand the nonlinear dispersion in the medium and physical phenomena such as the focusing, defocusing, splitting, and shifting of the light transmission, we present the spatial light propagation equations for the probe transmission signal and the four-wave mixing signal that result from self-phase modulation and cross-phase modulation. The propagation equation corresponding to the probe transmission signal is shown below:

$$\frac{\partial u_\mathrm{P}}{\partial Z}-\frac{\mathrm{i}\partial^2 u_\mathrm{P}}{2\partial\xi^2}=\frac{\mathrm{i}k_\mathrm{p}^2\omega_0^2 I}{n_0}\left(n_2^{S1}|u_\mathrm{P}|^2+2n_2^{X1}|u_1|^2+2n_2^{X2}|u_2|^2+2n_2^{X3}|u_3|^2+2n_2^{X4}|u_{3'}|^2\right)u_\mathrm{P}. \tag{1}$$

The generation of the four-wave mixing signal needs to satisfy the wave vector phase matching condition $k_\mathrm{F}=k_1+k_3-k_3'$, and the corresponding propagation equation is

$$\frac{\partial u_\mathrm{F}}{\partial Z}-\frac{\mathrm{i}\partial^2 u_\mathrm{F}}{2\partial\xi^2}=\frac{\mathrm{i}k_\mathrm{F}^2\omega_0^2 I}{n_0}\left(n_2^{S1}|u_\mathrm{F}|^2+2n_2^{X5}|u_1|^2+2n_2^{X6}|u_2|^2+2n_2^{X7}|u_3|^2+2n_2^{X8}|u_{3'}|^2\right)u_\mathrm{F}, \tag{2}$$

where $Z=z/\bar{L}$, $\bar{L}=k_1\omega_0^2$ is the diffraction length, ω_0 is the spot size of the probe transmission light, k_i is the wave vector of the laser field $\boldsymbol{E}_i$, ω_i is the frequency of $\boldsymbol{E}_i$ (where $i=1,2,3,3'$), z is the longitudinal coordinate in the propagation direction, Z is the normalized longitudinal length, and

$\xi = x/\omega_0$ and $\xi = y/\omega_0$ denote the transverse or longitudinal coordinates shown in Fig. 1(c), respectively; $k_{\rm P}$ is the wave vector of the probe transmission signal, $k_{\rm F}$ is the wave vector of the four-wave mixing signal, and $k_{\rm P} = k_{\rm F} = \omega_1 n_0/c$, where n_0 is the linear Kerr refractive index. n_2^{S1} represents the self-Kerr nonlinear coefficient of the probe transmission signal $\boldsymbol{E}_{\rm P}$, and n_2^{S2} denotes the self-Kerr nonlinear coefficient of the four-wave mixing signal $\boldsymbol{E}_{\rm F}$. n_2^{X1-X8} denotes the cross-Kerr nonlinear coefficients of the probe transmission signal $\boldsymbol{E}_{\rm P}$ as well as the four-wave mixing signal $\boldsymbol{E}_{\rm F}$ caused by $\boldsymbol{E}_1$, $\boldsymbol{E}_2$, $\boldsymbol{E}_3$, and $\boldsymbol{E}_3'$. $u_{\rm P} = E_{\rm P}/I_{\rm P}^{1/2}$, $u_1 = E_1/I_i^{1/2}$, $u_2 = E_2/I_i^{1/2}$, $u_3 = E_3/I_i^{1/2}$, $u_{\rm F} = E_{\rm F}/I_{\rm F}^{1/2}$ and $u_3' = E_3'/I_i^{1/2}$ represent the normalization of the two different signal values $\boldsymbol{E}_{\rm P}$ and $\boldsymbol{E}_{\rm F}$. Here, we assume that the intensities of the laser fields $\boldsymbol{E}_1$, $\boldsymbol{E}_2$, $\boldsymbol{E}_3$, and $\boldsymbol{E}_3'$ are denoted by the symbol I_i, where $i = 1,2,3,3'$, respectively. The purpose of this notation is to further differentiate them without creating a substantial impact on the theoretical model under discussion.

In the left-hand sides of Eqs. (1) and (2), the first terms describe the longitudinal propagation process of the probe signal and the four-wave mixing signal, respectively. The second terms reflect the diffraction phenomena of the two different laser fields during the propagation process. In the right-hand sides of the two equations, the first terms describe the nonlinear self-Kerr effect, and the second through the fifth terms describe the nonlinear cross-Kerr effect.

For the specific application of the Kerr effect in this experiment, all nonlinear Kerr effects can be expressed in a generalized form as

$$n_2 \approx \frac{\mathrm{Re}\,\tilde{\rho}_{10}^{(3)}}{\varepsilon_0 c n_0}, \tag{3}$$

where ε_0 is the dielectric constant, c is the speed of light in vacuum, and $\tilde{\rho}_{10}^{(3)}$ is the third-order density matrix,[21] which can be obtained by solving the coupled density matrix equations. According to the atomic energy levels and the Liouville path,[22] it is known that when no laser field is added, the system state can be represented by the density matrix $\rho_{00}^{(0)}$. When $\boldsymbol{E}_1$ is added, the system state changes to $\rho_{00}^{(0)} \xrightarrow{\omega_1} \rho_{10}^{(1)}$, which results in the first-order density matrix $\rho_{10}^{(1)} = \mathrm{i}G_1/d_1$. After $\boldsymbol{E}_3$, $\boldsymbol{E}_3'$, and $\boldsymbol{E}_2$ are added, the three optical fields simultaneously produce the dressing effect on energy level $|1\rangle$, which affects the Liouville path and changes the first-order density matrix. The new first-order density matrix expression is as follows:

$$\rho_{10}^{(1)} = \frac{\mathrm{i}G_1}{d_1 + |G_{3\rm s}|^2/d_3 + |G_2|^2/d_2}. \tag{4}$$

Based on the first-order density matrix, the third-order density matrix expression can be obtained according to the Liouville path $\rho_{00}^{(0)} \xrightarrow{\omega_1} \rho_{10}^{(1)} \xrightarrow{\omega_3'} \rho_{30}^{(2)} \xrightarrow{\omega_3} \rho_{10}^{(3)}$:

$$\tilde{\rho}_{10}^{(3)} = \frac{-\mathrm{i}G_1 G_3 G_3'}{(d_1 + |G_{3\rm s}|^2/d_3 + |G_2|^2/d_2)^2 d_3}, \tag{5}$$

where $|G_{3\rm s}|^2 = |G_3|^2 + |G_3'|^2 + 2G_3G_3'\cos(2k_c z)$, $d_1 = \Gamma_{10} + \mathrm{i}\Delta_1$, $d_3 = \Gamma_{30} + \mathrm{i}\Delta_1 - \mathrm{i}\Delta_3$, and $d_2 = \Gamma_{20} + \mathrm{i}\Delta_1 + \mathrm{i}\Delta_2$. $G_i = \mu_i E_i/\hbar$ is the Rabi frequency, μ_i is the dipole moment, $k_c = (\omega_3 + \omega_3')/2c$, the frequency detuning $\Delta_i = \Omega_i - \omega_i$ (Ω_i represents the resonant frequency excited by $\boldsymbol{E}_i$), and Γ_{ij} represents the transverse relaxation rate between the energy levels $|i\rangle$ and $|j\rangle$.

Equation (5) is the general third-order density matrix expression. This expression is slightly different due to the individual subterms that appear due to the effects of different dressing fields. Therefore, there are slight differences in the self-Kerr nonlinear effects caused by the probe transmission signal and the four-wave mixing signal. Similarly, the cross-Kerr nonlinear effect exhibits slight differences because of laser beams $\boldsymbol{E}_1$, $\boldsymbol{E}_2$, $\boldsymbol{E}_3$, and $\boldsymbol{E}_3'$. In fact, the nonlinear Kerr effect is formed by superposition, where $n_2^{S1,2} = n_2^{SE}$, $n_2^{X1,5} = n_2^{XE_1}$, $n_2^{X2,6} = n_2^{XE_2}$, $n_2^{X3,7} = n_2^{XE_3}$, and $n_2^{X4,8} = n_2^{XE_3'}$. Without taking into account the effects of laser beam diffraction and cross-phase modulation, the solutions of Eqs. (1) and (2) can be expressed as

$$\mu_{\rm P,F}(z,\xi) = \mu_{\rm P,F}(0,\xi)\Sigma_i \exp \mathrm{i}\varphi_i, \tag{6}$$

where $i = 1,2,3$, $\phi_i = 2k_{\rm P,F} z n_2^{XE_I} I_i \mathrm{e}^{-(\xi-\xi_i)^2/2}/(n_0 I_{\rm P,F})$ denotes the nonlinear phase shifts caused by the laser fields $\boldsymbol{E}_i$, respectively, and ξ_i is the position of the central coordinate of $\boldsymbol{E}_i$ in the cross section, which is used as the original central coordinate of the corresponding probe transmission signal as well as the four-wave mixing signal. Based on this, we set the transverse or longitudinal propagating wave vector of the external dressing field introduced by $\boldsymbol{E}_i$ to $\delta k_{i\xi}' = (\partial\varphi_i/\partial\xi)\hat{\xi}$, where $\hat{\xi}$ is the unit vector in the direction of the transverse or longitudinal axis. Since the change in phase shift is mainly observed in the cross-sectional direction of the laser field, the direction of $\delta k_{i\xi}'$ determines the spatial variation characteristics of the probe transmission signal and the four-wave mixing signal in the cross-sectional direction. For example, $\delta k_{p,3x}' > 0$ denotes the inductive effect of the $\boldsymbol{E}_3$ field on the probe transmission signal in the x-axis direction. When $n_2^{x_i} > 0$, $\delta k_{i\xi}'$ always points to the center of the laser beam, and the corresponding weak beam continuously moves toward the strong beam. When $n_2^{x_i} < 0$, the weak beam exhibits a state of deviation from the strong beam. When $n_2^{s_i} > 0$, the weak beam exhibits a focusing phenomenon. When $n_2^{s_i} < 0$, the weak beam exhibits a defocusing phenomenon. To facilitate the subsequent study of the stronger spatial focusing or defocusing characteristics arising from the nonlinear phase shift at lower intensities, a

general theoretical expression for the nonlinear refractive index is given as

$$\Delta n_2^{E_i} = n_2^{E_i} I_i, \quad (i = 1, 2, 3, 3'). \tag{7}$$

In addition, when the nonlinear refractive index is large and the field strength is low, we can also use Eq. (7) to theoretically approximate the nonlinear phase shift and strong spatial focusing or defocusing phenomenon in order to simplify this complex problem.

4. Experimental results

First of all, the spectrums and spatial images of the probe transmission signal and four-wave mixing signal are obtained using frequency detunings of Δ_2 and Δ_3, both at 400 MHz, and a scanning frequency detuning Δ_1 in the range of -800 MHz to 800 MHz. Figures 2(a1) and 2(a2) show the spectral variations of the probe transmission signal and the four-wave mixing signal, respectively. As shown in Fig. 2(a1), when the scanning frequency detuning $\Delta_1 = -400$ MHz, a peak is observed in the probe transmission signal, which is the EIT generated by the laser fields $\boldsymbol{E}_1$ and $\boldsymbol{E}_3$, $\boldsymbol{E}_3'$, and $\boldsymbol{E}_2$. This can be compared with the spectrum of the four-wave mixing signal at the same frequency detuning position in Fig. 2(a2): A four-wave mixing signal peak can be observed, which is generated by the laser field $\boldsymbol{E}_1$ and the coupling laser fields $\boldsymbol{E}_3$ and $\boldsymbol{E}_3'$ interacting under the phase-matching condition $k_{\mathrm{F}} = k_1 + k_3 - k_3'$. Figure 2(a3) is a diagram of the relationship between the scanning frequency detuning Δ_1 and the nonlinear refractive index $\Delta n_2^{XE_1}$ theoretically simulated according to Eqs. (5) and (7). It can be observed that the nonlinear refractive index changes with the scanning frequency detuning Δ_1. At the position of $\Delta_1 = -400$ MHz, in particular, the nonlinear refractive index is dressed by $\boldsymbol{E}_2$, forming a suppression pit. The reason for this is that at $\Delta_1 = -400$ MHz, $\boldsymbol{E}_1$ resonates with $\boldsymbol{E}_2$, causing the subterm $|G_2|^2/d_2$ in Eq. (5) to increase and $\tilde{\rho}_{10}^{(3)}$ to decrease. From Eqs. (3) and (7) it can be seen that n_2 is directly proportional to $\tilde{\rho}_{10a}^{(3)}$ and $\Delta n_2^{E_i}$ is directly proportional to $n_2^{E_i}$. Therefore, the nonlinear Kerr refractive index decreases by a certain degree at $\Delta_1 = -400$ MHz. From the perspective of the nonlinear refractive index change, the change in the spot can be quantitatively described to investigate the variations of the spatial images of both signals. The nonlinear Kerr refractive index $\Delta n_2^{E_1}$ is calibrated to be zero at the scanning frequency detuning of $\Delta_1 = 0$ MHz, where the light field $\boldsymbol{E}_1$ is at the resonant position of the atomic energy level. Figure 2(b1) shows the spatial image variation of the probe transmission signal. When the scanning frequency detuning is $\Delta_1 < 0$ MHz, the nonlinear Kerr refractive index Δn_2 is greater than zero, as shown in Fig. 2(a3). The theoretical expression of the nonlinear refractive index according to Eq. (7) shows that the transverse propagation wave vector $\delta k'_{p,1\xi}$ always points to the center of the laser beam at this moment, so the spatial spot of the probe transmission signal exhibits a focused state. When the scanning frequency detuning Δ_1 changes, the nonlinear Kerr refractive index also increases. When the scanning frequency detuning is $\Delta_1 = -100$ MHz, the nonlinear Kerr refractive index reaches its maximum. From Fig. 2(b1), it can be learned that with the progression of the above process, the focusing phenomenon in the spatial image of the probe transmission signal also increases and peaks when $\Delta_1 = -100$ MHz. When the scanning frequency detuning is $\Delta_1 > 0$ MHz, the value of the nonlinear Kerr refractive index Δn_2 becomes less than zero, and the point denoted by $\delta k'_{p,1\xi}$ gradually deviates from the center of the beam. At this moment, the spatial image of the probe transmission signal is gradually transformed from focused to defocused. When the scanning frequency detuning Δ_1 is increased, the absolute value of the nonlinear Kerr refractive index appears to first increase before gradually decreasing. At the same time, the corresponding spot of the probe transmission signal remains defocused. Figure 2(b2) shows the spatial image variation of the four-wave mixing signal. Compared with the probe transmission signal in Fig. 2(b1), the four-wave mixing signal shows the same spot focus as the probe transmission signal when the scanning frequency detuning $\Delta_1 < 0$. This phenomenon appears because the generation of the four-wave mixing signal mainly depends on $\boldsymbol{E}_1$. In addition, its focusing and defocusing phenomena also depend on the nonlinear refractive index $\Delta n_2^{E_1}$ caused by $\boldsymbol{E}_1$. When the scanning frequency detuning is $\Delta_1 > 0$ MHz, the nonlinear Kerr refractive index is less than zero. Meanwhile, the four-wave mixing signal is similarly gradually transformed from focused to defocused. The four-wave mixing signal differs from the probe

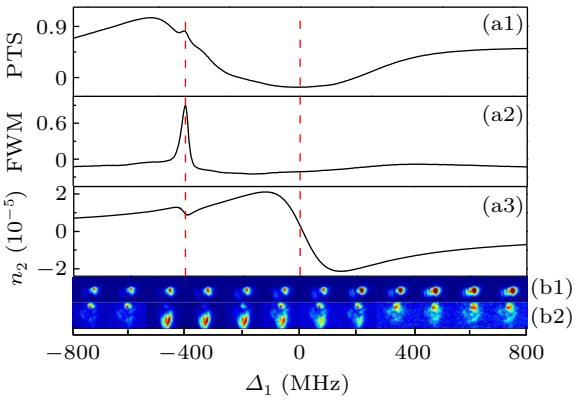


Fig. 2. Probe transmission spectra (a1), four-wave mixing spectra (a2), and refractive index (a3) with scanning detuning Δ_1 in the range of -800 MHz to 800 MHz. Spatial image of the probe transmission signal (b1) and a spatial image of the four-wave mixing signal (b2) with scanning detuning Δ_1 in the range of -800 MHz to 800 MHz. In the above figures, the coupling field detuning Δ_3 and the dressing field detuning Δ_2 are both 400 MHz, the power of $\boldsymbol{E}_1$ is 1.5 mW, the power of $\boldsymbol{E}_3$ is 15 mW, the power of $\boldsymbol{E}_3'$ is 15 mW, and the power of $\boldsymbol{E}_2$ is 30 mW.

transmission signal in that the spatial image of the four-wave mixing signal undergoes a significant spatial shift in the y direction. This difference is caused by the nonlinear phase shift resulting from the effect of the vertical component of the light field $\boldsymbol{E}_1$ on the medium. The results show that the self-Kerr effect caused by the probe field $\boldsymbol{E}_1$ can modulate the spatial light spot of the probe transmission signal and the four-wave mixing signal in a certain range by changing the nonlinear Kerr refractive index.

We now focus on the modulation of the spatial images by narrowing Δ_1 in the vicinity of the generated EIT and four-wave mixing under the cross-Kerr effect of the four beams interacting with each other. To ensure the symmetry of the study, we change the frequency detuning Δ_3 to -400 MHz and observe the variation of both signals under different experimental conditions by controlling a single variable. Figure 3(a1) shows the spectrum of the probe transmission signal for the scanning frequency detuning Δ_1. On comparing this with Fig. 2(a1), it can clearly be observed that when Δ_3 changes from positive to negative, the spectrum of the probe signal generates electromagnetically induced transparency at the scanning frequency detuning of $\Delta_1 = 430$ MHz. Figure 3(a2) shows the spectrum of the four-wave mixing signal for the scanning frequency detuning Δ_1. Similarly, comparing Fig. 3(a2) with Fig. 2(a2), one can see that the spectra of both figures show basically the same pattern at symmetric frequencies. The theoretical variation curve of the Kerr nonlinear refractive index under the effect of light field $\boldsymbol{E}_1$ alone is shown in Fig. 3(a3), which demonstrates that the variation in the Kerr nonlinear refractive index only occurs with the scanning frequency detuning.

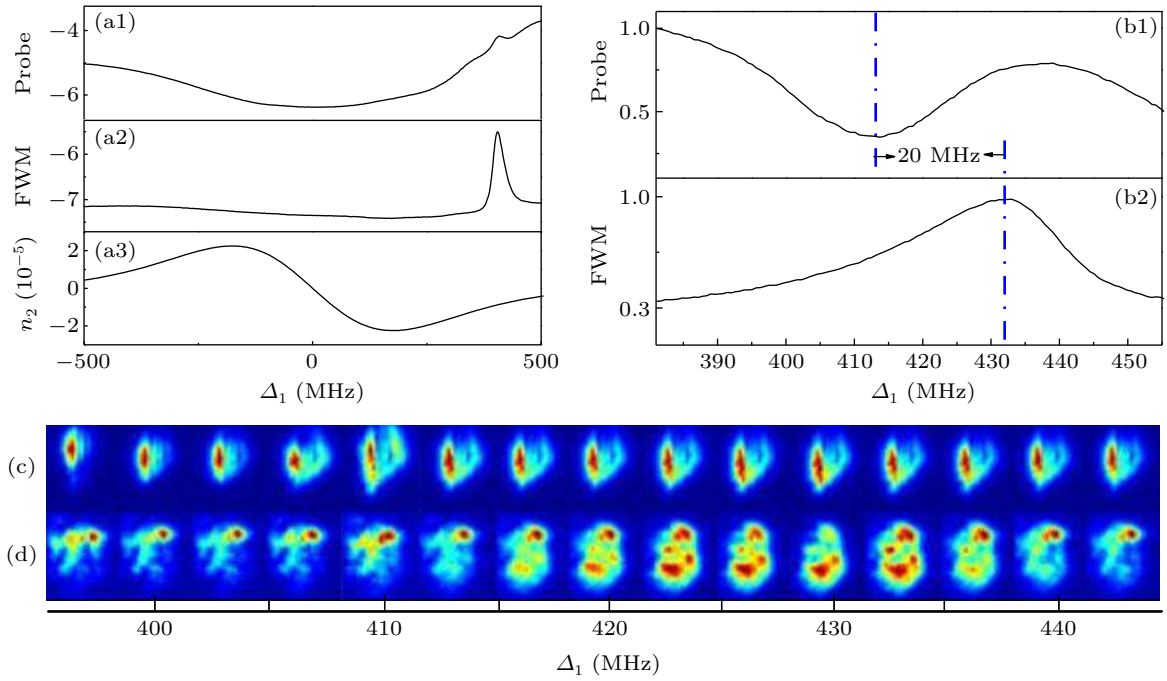


Fig. 3. Probe transmission spectra (a1), four-wave mixing spectra (a2), and refractive index (a3) with scanning frequency detuning Δ_1 in the range of -500 MHz to 500 MHz. Spatial images of the probe transmission signal (b1) and the four-wave mixing signal (b2) with scanning frequency detuning Δ_1 in the range of 400 MHz to 440 MHz. In the above figures, the coupling field frequency detuning Δ_3 and the dressing field frequency detuning Δ_2 are both -400 MHz, the $\boldsymbol{E}_1$ power is 1.5 mW, the $\boldsymbol{E}_3$ power is 15 mW, and the $\boldsymbol{E}_3'$ power is 15 mW. All spectral vertical axis units are normalized units (arb. units).

The reduced ranges of the spectral signals in Figs. 3(a1) and 3(a2) are further amplified, as shown in Figs. 3(b1) and 3(b2), respectively. Figures 3(c) and 3(d) show the spatial image evolutions of the corresponding probe transmission signal and four-wave mixing signal after the range of scanning frequency detunings Δ_1 is reduced to the defocus area. By comparing Figs. 3(c) and 3(d), it can be seen that the spatial images of both the probe transmission signal and the four-wave mixing signal produce the splitting phenomenon in the x- and y-axis directions, which is caused by different nonlinear phase shifts between each light field and the medium. The probe transmission signal is dressed in the x-axis direction by $\boldsymbol{E}_3$ and $\boldsymbol{E}_3'$. The effect of the two beams is caused by the same light intensity, which results in $\phi_3 - \phi_3' = 0$. Hence, in the propagation of the corresponding signal light, the nonlinear phase shift in the transverse or longitudinal components of $\boldsymbol{E}_1$ and $\boldsymbol{E}_2$ leads to changes in the propagation wave vectors $\delta k'_{p,1\xi} = (\partial\varphi_1/\partial\xi)\hat{\xi}$ and $\delta k'_{p,2\xi} = (\partial\phi_2/\partial\xi)\hat{\xi}$, which play important roles in the propagation process. As a result, the probe transmission signal images produce the splitting phenomenon in both the x- and y-axis directions. However, the light fields $\boldsymbol{E}_1$ and $\boldsymbol{E}_2$ are oppositely incident, so that part of the transverse component is balanced. Thus, in the spatial image, the longitudinal splitting is more obvious than the transverse splitting. By the same token, the four-wave mixing signal is mainly affected by the light fields $\boldsymbol{E}_1$

and $\boldsymbol{E}_2$, which leads to splitting of the transverse and longitudinal spatial images. Due to the weaker four-wave mixing signal, however, the nonlinear phase shift caused in the four-wave mixing signal by each light field is larger than that of the probe transmission signal. As such, the longitudinal splitting is larger, so that the transverse splitting in Fig. 3(d) is not sufficiently obvious. Based on the spatial images in Figs. 3(c) and 3(d), it can be seen that when Δ_1 scans at about 410 MHz, the probe transmission signal is suppressed and reaches a trough. Meanwhile, the spatial image of the probe transmission signal splits by the maximum amount in the x-axis direction. When Δ_1 scans at about 430 MHz, the four-wave mixing signal reaches its peak value. At the same time, the splitting of the four-wave mixing signal in the y-axis direction is slightly suppressed. By comparing these two signals, it can be found that there is a difference of 20 MHz between the positions where the spatial images change the most due to the dressing effect. This is because when $\Delta_1 = 410$ MHz, the signal strength $I_{\rm P}$ of the probe transmission signal $\boldsymbol{E}_{\rm P}$ is at its minimum. Meanwhile, the corresponding nonlinear phase shift $\phi_i = 2k_{\rm P,F}zn_2^{XE_i}I_1{\rm e}^{-(\xi-\xi_1)^2/2}/(n_0I_{\rm P,F})$ is at its maximum. Therefore, the splitting of the probe transmission signal here is at its maximum along the x-axis. When $\Delta_1 = 430$ MHz, the signal intensity $I_{\rm F}$ of the four-wave mixing signal $\boldsymbol{E}_{\rm F}$ is at its maximum. Meanwhile, the corresponding nonlinear phase shift $\phi_i = 2k_{\rm P,F}zn_2^{XE_i}I_1{\rm e}^{-(\xi-\xi_1)^2/2}/(n_0I_{\rm P,F})$ is at its minimum. Therefore, the splitting of the four-wave mixing signal along the y-axis direction is slightly suppressed here.

This section describes the modulation effect of the nonlinear cross-Kerr effect on the signal, which was observed by scanning the frequency detuning Δ_2 and altering the intensity of the probe field. Fixing $\Delta_1 = 200$ MHz allows the frequency detuning Δ_2 to be scanned while changes in the images are located within the defocused area, which facilitates a more intuitive observation of the effect of the external dressing field. Figures 4(a1) and 4(a2) show the spectral variations and the spatial images of the probe transmission signal for a dressing field $\boldsymbol{E}_2$ power of 30 mW. Theoretically, when the probe transmission signal satisfies the resonance condition of $\Delta_1 + \Delta_2 = 0$ MHz, it should generate an EIT peak. However, when the probe field $\boldsymbol{E}_1$ power is large, its interaction with the dressing field $\boldsymbol{E}_2$ is strong, so that $\boldsymbol{E}_2$ has a suppressing effect on the energy level $|1\rangle$. Therefore, at a scanning frequency detuning of $\Delta_2 = 0$ MHz, a suppression phenomenon occurs in the middle of the EIT peak, because the $|G_2|^2/d_2$ term in Eq. (5) causes the dressing field $\boldsymbol{E}_2$ to produce a dressing effect on the probe transmission signal. As we can see from the spatial image of the probe transmission signal in Fig. 4(a2), the $\boldsymbol{E}_2$ field has a clear suppressive effect on the probe transmission signal. Figures 4(a1′) and 4(a2′) show this phenomenon after only reducing the power of $\boldsymbol{E}_1$ and keeping all the other conditions constant. The probe transmission signal at this time shows a typical single-peak spectrum, because the field power of $\boldsymbol{E}_1$ is too small and the interaction with $\boldsymbol{E}_2$ is weak. Therefore, the suppressive effect of $\boldsymbol{E}_2$ on $\boldsymbol{E}_1$ cannot be reflected in the figure. On comparing Fig. 4(a2′) with Fig. 4(a2), it can be seen more obviously that with a continuous change of the scanning frequency detuning Δ_2, the intensities of the probe transmission signal, spot area, and spot brightness decrease when the intensity of the probe field diminishes. In addition, hardly any obvious change can be seen in the spatial image in the weak signal case. Correspondingly, the strong probe field case shows significant transverse and longitudinal splitting of the probe transmission image, for the same reasons as explained above.

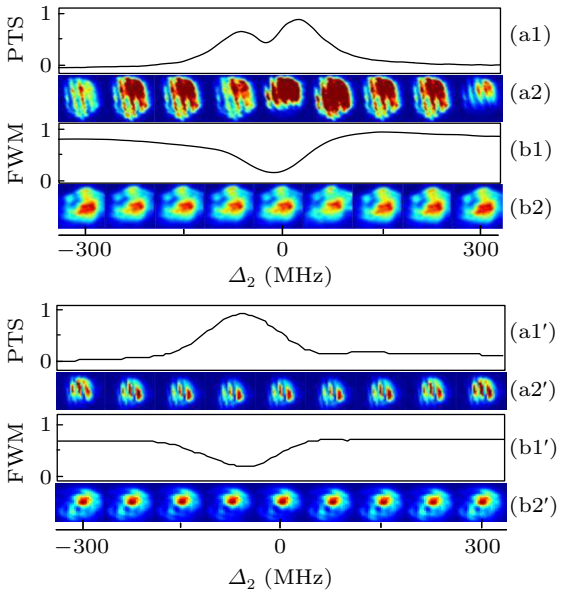


Fig. 4. (a) Scanning of the frequency detuning Δ_2 in the range of -300 MHz to 300 MHz: the probe transmission spectrum (a1) and the corresponding spatial images (a2) at a probe field $\boldsymbol{E}_1$ power of 2 mW; the probe transmission spectrum (a1′) and the corresponding spatial images (a2′) at an $\boldsymbol{E}_1$ power of 1 mW, (b) scanning frequency detuning Δ_2 in the range of -300 MHz to 300 MHz: the four-wave mixing spectrum (b1) and the corresponding spatial images (b2) at a probe field $\boldsymbol{E}_1$ power of 2 mW; the four-wave mixing signal spectrum (b1′) and the corresponding spatial images (b2′) at an $\boldsymbol{E}_1$ power of 1 mW. All spectral vertical axis units are normalized units (arb. units).

The spectral and spatial image changes of the four-wave mixing signal are shown in Figs. 4(b1) and 4(b2), respectively, for an $\boldsymbol{E}_1$ field power of 2 mW. In the spectrum of the four-wave mixing signal, it can clearly be seen that the four-wave mixing signal is also affected by the dressing effect of $\boldsymbol{E}_2$, which results in a suppression pit at $\Delta_2 = 0$ MHz in the spectrum. From Fig. 4(b2), it can be observed that due to the cooperative effect of the nonlinear phase shifts φ_1 and φ_2 caused by $\boldsymbol{E}_1$ and $\boldsymbol{E}_2$, the spatial image of the four-wave mixing signal exhibits a splitting phenomenon. Additionally, the variation of the frequency detuning of $\boldsymbol{E}_2$ changes the combined nonlinear refractive index of the two light fields. It turns out that if the change in the intensity is weak, the degree of splitting does

not change with Δ_2, indicating that the nonlinear modulation is subject to a smaller $\boldsymbol{E}_2$ effect.

The spectral and spatial image changes of the four-wave mixing signal after decreasing the power of $\boldsymbol{E}_1$ to 1 mW are shown in Figs. 4(b1′) and 4(b2′), respectively. In comparison with Fig. 4(b1), we still see a suppression pit, but its depth is smaller than in Fig. 4(b1′). Figure 4(b2′) shows the corresponding spatial image of the four-wave mixing signal. On compared this with Fig. 4(b2), it can be seen that the image does not split longitudinally after the $\boldsymbol{E}_1$ power is reduced. This indicates that the image of the four-wave mixing signal splits longitudinally due to the high power of $\boldsymbol{E}_1$. Furthermore, the main reason for this is the y-axis component of the nonlinear phase shift caused by the interaction between $\boldsymbol{E}_1$ and the atomic medium. This demonstrates that different probe field powers play a crucial role in the splitting modulation of the probe transmission and four-wave mixing images.

Finally, we further investigated the relationship between the intensity of the external dressing field and the nonlinear refractive index by fixing $\Delta_1 = 200$ MHz in the defocused area. The spatial evolution patterns of the four-wave mixing images are shown in Fig. 5(a). Spatial images are shown in detail in Figs. 5(a1), 5(a2), and 5(a3), for different powers of the external dressing field $\boldsymbol{E}_2$ of 30 mW, 20 mW, and 10 mW, respectively. In the transverse view, the optical spot area of the four-wave mixing decreases near $\Delta_2 = 0$ MHz, which is consistent with the intensity magnitude of the spectral signals in Figs. 5(b1), 5(b2), and 5(b3). In the longitudinal view, the suppression effect of the light field $\boldsymbol{E}_2$ on the four-wave mixing signal is smaller away from the resonant frequency of 0 MHz. In the other words, for the same scanning frequency detuning, the smaller the power, the smaller the area of the optical spot that appears. Moreover, the farther Δ_2 is from 0 MHz, the more apparent this pattern becomes. When Δ_2 is closer to resonant frequency of 0 MHz, the larger the $\boldsymbol{E}_2$ power becomes, and the spot area shows the opposite pattern. To be precise, the closer Δ_2 is to 0 MHz, the larger the $\boldsymbol{E}_2$ light-field power becomes, and the smaller the spot appears due to the suppression effect. This is because when $\Delta_2 = 0$ MHz, the resonance effect between $\boldsymbol{E}_2$ and the atomic energy level is at its strongest, and the dressing effect of $\boldsymbol{E}_2$ on the four-wave mixing signal exhibits stronger suppression. Figure 5(b) shows the pattern of variation in the spectrum intensity of the four-wave mixing signal for various powers. The larger the $\boldsymbol{E}_2$ power, the more significant the suppression effect on the four-wave mixing spectrum becomes, and the deeper the suppression pit. In Figs. 5(a1) and 5(b1), it can be seen that the power of $\boldsymbol{E}_2$ is 30 mW. Under these conditions, with a changing scanning frequency detuning Δ_2, the suppression pit created by the four-wave mixing signal at $\Delta_2 = 0$ MHz corresponds to the smallest spot in Fig. 5(a1). As the power of $\boldsymbol{E}_2$ decreases, the suppression of the four-wave mixing signal by $\boldsymbol{E}_2$ diminishes, and the suppression pit depth becomes smaller, as shown in Figs. 5(b2) and 5(b3). In Figs. 5(a2) and 5(a3), when $\Delta_2 = 0$ MHz and the dressing effect is the strongest, the smaller the power of $\boldsymbol{E}_2$, the larger the optical spot. For a more intuitive observation of the relationship between the intensity of the dressing field and the variation of the optical spot, we have added a red dashed line as a reference in Fig. 5(a). The dashed line corresponds to the location of the maximum intensity of the dressing field. It can be seen that when the $\boldsymbol{E}_2$ power is constant, the area of the optical spot shrinks to its minimum when the dressing effect reaches its maximum. Moreover, the optical spot is increasingly less suppressed by $\boldsymbol{E}_2$ as the $\boldsymbol{E}_2$ power decreases. At the same time, the spot area gradually increases at the same scanning frequency detuning. Figure 5(c) shows the trend of the nonlinear Kerr refractive index at different dressing intensities. As the scanning frequency detuning Δ_2 changes, the refractive index gradually changes from zero to less than zero and then back to its initial position. In addition, the larger the power of $\boldsymbol{E}_2$, the larger the change in the Kerr refractive index becomes, and the greater the variations of the curves corresponding to Fig. 5(c1), 5(c2), and 5(c3).

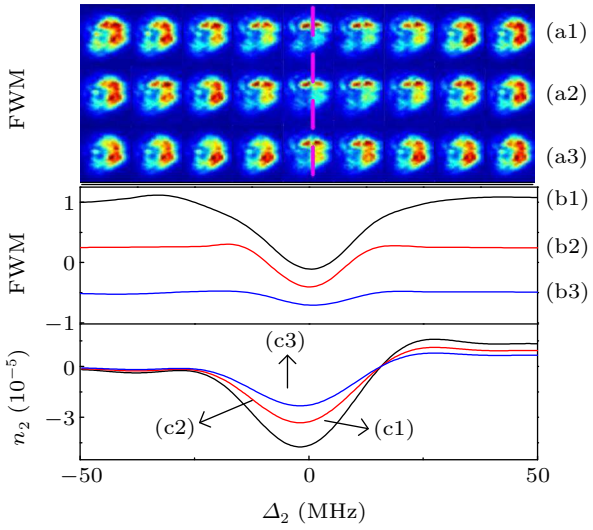


Fig. 5. (a) Spatial images of the four-wave mixing signal with a scanning frequency detuning Δ_2 range of −50 MHz to 50 MHz, an $\boldsymbol{E}_1$ power of 1.5 mW, and dressing field intensities of (a1) 30 mW, (a2) 20 mW, and (a3) 10 mW, respectively. (b) Spectra of the four-wave mixing with a scanning frequency detuning Δ_2 range of −50 MHz to 50 MHz and dressing field intensities of (b1) 30 mW, (b2) 20 mW, and (b3) 10 mW, respectively. (c) Nonlinear refractive index variation for a scanning frequency detuning Δ_2 range of −50 MHz to 50 MHz and dressing field intensities of (c1) 30 mW, (c2) 20 mW, and (c3) 10 mW, respectively. The power of $\boldsymbol{E}_3$ is 15 mW, and the power of $\boldsymbol{E}_3'$ is 15 mW.

Based on Figs. 5(a)–5(c) it can be seen that the external dressing field has a modulating effect on the nonlinear Kerr refractive index. Furthermore, it may also modulate the intensity and spatial spot area of the four-wave mixing signal. When the intensity of the external dressing field is larger, the nonlinear Kerr refractive index changes at a faster rate, and

the nonlinear modulating effect of the four-wave mixing signal becomes stronger. Conversely, when the intensity of the external dressing field is smaller, the nonlinear Kerr refractive index changes more slowly, and the modulating effect of the four-wave mixing signal becomes weaker.

5. Conclusion

In summary, we have presented a theoretical and experimental study of the spatial image and spectral signal evolution patterns of the probe transmission and the four-wave mixing signal based on an inverted Y-type four-energy level atomic system by changing the adjustable parameters of the light field. The refractive index of the medium was modulated by the nonlinear Kerr effect of the interaction between the light field and the atomic medium. In addition, the nonlinear phase shift of the probe transmission and the four-wave mixing signal was modulated. Spatial shifting and splitting patterns of the probe transmission and the four-wave mixing signals were obtained by manipulating the light fields. In this process, it was observed that frequency detuning and the power of the light fields play a decisive role in the spatial image change of the probe transmission and four-wave mixing signals. These modulating patterns provide experimental technology support for all-optical communications and open up potential research prospects for nonlinear optical communications networks.

Acknowledgments

Project supported by the National Natural Science Foundation of China (Grant No. 61705182) and the Natural Science Foundation of Shaanxi Province, China (Grant No. 2017JQ6024).

References

[1] Jia R C, Ren Y Y, Zhao X J and Chen F 2021 *Chin. Opt. Lett.* **19** 060013
[2] Hennessy T and Busch T 2014 *Opt. Express* **22** 32509
[3] Wang D, Wu J Z and Zhang J X 2016 *Chin. Phys. B* **25** 064202
[4] Lourdesamy J P, Runge A F J, Alexander T J, Hudson D D, Blanco R A and Sterke C M D 2021 *Nat. Phys.* **18** 59
[5] Harris S E, Field J E and Imamoğlu A 1990 *Phys. Rev. Lett.* **64** 1107
[6] Boller K J, Imamoğlu A and Harris S E 1991 *Phys. Rev. Lett.* **66** 2593
[7] Ogura I, Kurita H, Sasaki T and Yokoyama H 2001 *Opt. Quantum Electron.* **33** 709
[8] Brown A W and Xiao M 2005 *Opt. Lett.* **30** 699
[9] Li C B, Zheng H B, Zhang Y P, Nie Z Q, Song J P and Xiao M 2009 *Appl. Phys. Lett.* **95** 041103
[10] Li Y Q and Xiao M 1996 *Opt. Lett.* **21** 1064
[11] Li Y Y, Li L, Zhang Y Z and Zhang L 2019 *Chin. Phys. B* **28** 104201
[12] Petrenko A D 1999 *Phys. Solid State* **41** 591
[13] Wang J, Sheng A G, Huang X, Li R Y and He G Q 2020 *Chin. Phys. B* **29** 034207
[14] Dong Y B, Li J Y and Zhou Z Y 2017 *Chin. Phys. B* **26** 014202
[15] Zhang Y P, Wang Z G, Nie Z Q, Li C B, Chen H X, Lu K Q and Xiao M 2011 *Phys. Rev. Lett.* **106** 093904
[16] Wang Z G, Gao M Q, Abdul R M and Zhang Y P 2016 *Sci. Rep.* **6** 28185
[17] Artoni M and Rocca G C L 2006 *Phys. Rev. Lett.* **96** 073905
[18] Savotchenko S E 2021 *Opt. Quantum Electron.* **53** 1
[19] Liu X Y, Zhao X, Sun J F, Xu Z and Hu Z F 2021 *Chin. Phys. B* **30** 083203
[20] Hao L P, Xue Y M, Fan J B, Jiao Y C, Zhao J M and Jia S T 2019 *Chin. Phys. B* **28** 053202
[21] Al-Nashy B and Al-Khursan A H 2009 *Opt. Quantum Electron.* **41** 989
[22] Harlow D, Martz J and Witten E 2011 *J. High Energy Phys.* **2011** 71